Establishing self-dopant design principles from structure-function relationships in self-n-doped perylene diimide organic semiconductors

Daniel Powell[1], Xueqiao Zhang[2], Chideraa I. Nwachukwu[1], Edwin J. Miller[1], Kameron R. Hansen[1], Laura Flannery[1], Jonathan Ogle[1], Alex Berzansky,[1] John G. Labram[2], Andrew G. Roberts[1], Luisa Whittaker-Brooks[1,*]

1. *Department of Chemistry, University of Utah, Salt Lake City, UT 84112, USA*

2. *School of Electrical Engineering and Computer Science, Oregon State University, Corvallis, OR 97331, USA*

ABSTRACT

Self-doping is a particular doping method that has been applied to a wide range of organic semiconductors. However, there is a lack of understanding regarding the relationship between dopant structure and function. We investigated a structurally diverse series of self-n-doped perylene diimides (PDIs) to study the impact of steric encumbrance, counterion selection, and dopant/PDI tether distance on functional parameters such as doping, stability, morphology, and charge carrier mobility. Our studies show that self-n-doping is best enabled by the use of sterically encumbered ammoniums with short tethers and Lewis basic counterions. Additionally, water is found to inhibit doping, leading us to conclude that thermal degradation is merely a phenomenological feature of certain dopants, and that residual solvent evaporation is the primary driver of thermally activated doping. In-situ grazing incidence wide-angle X-ray scattering studies show that sample annealing increases the π-π stacking distance and shrinks grain boundaries for

improved long-range ordering. These features are then correlated to contactless carrier mobility measurements with time-resolved microwave conductivity before and after thermal annealing. The collective relationships between structural features and functionality are finally used to establish explicit self-n-dopant design principles for the future design of materials with improved functionality.

KEYWORDS: self-doping, spin concentrations, organic semiconductors, morphology, charge carrier mobility

INTRODUCTION

In 2000, Alan Heeger, Alan MacDiarmid, and Hideki Shirakawa were awarded the Nobel Prize in chemistry for their discovery and development of conducting polymers.[1] Their seminal research in 1977 showed that the electrical conductivity of polyacetylene increased over seven orders of magnitude when doping thin films with iodine vapor.[2] In the 1980s, as researchers began to devote serious focus to the development of functional organic semiconductors (OSCs), the field progressed to using dopants that were more stable and offered better control over the doping process. In 1987, Heeger's group developed the method known as self-doping in conductive polymers, wherein an ionizable functional group was covalently tethered to the host semiconductor.[3] Since then, numerous self-dopants have been reported as both n-type and p-type dopants. Though the utility of self-doping was immediately recognized, utilization of the method has grown substantially in recent years with increasing reports that evaluate and improve host/dopant miscibility. Indeed, self-dopants offer unique advantages over extrinsic dopants,[4] which must diffuse into the polymer matrix during the charge injection process. Poor diffusion or polarity mismatching may cause extrinsic dopants to aggregate, leading to phase-separated domains in the solid-state film.[5] Extrinsic dopants can also significantly alter polymer morphology

to be very different from that of the native polymer even at modest dopant concentrations,[6] making it difficult to deconvolute morphology from the electronic structure changes that result from doping. In contrast, self-dopants are included as a structural component of the polymer itself, which ensures a homogeneous dopant distribution and can improve morphological homogeneity. From the chemist's perspective, self-doping is a clever and convenient method of circumventing the laborious miscibility tailoring that is often required of materials that employ extrinsic dopants. As such, self-doping has been applied to a diverse range of polymer derivatives including polyaniline, polythiophenes, and others.[7]

Alongside the development of polymers, the organic electronics community has also been actively engaged in small molecule semiconductor research.[8] Small molecules present many unique advantages over polymers. Notably, polymer synthesis results in a distribution of tether lengths of differing molecular weights resulting in polydisperse matrices that, when cast into thin films, have varying density, unreacted sites, looping, and branching between weakly interacting polymer subunits with many degrees of conformational freedom.[9] Their solid-state microstructures can be likened to that of cooked spaghetti noodles on a plate. However, on a sufficiently large length scale, polymers are quite tolerant to this morphological disorder. The polymer strands form a complex meshed network containing highly ordered crystalline regions that are dominated by bandlike charge transport and are separated by domains of amorphous disorder where site-to-site hopping prevails, leading charge carriers to percolate between these regions.[6,10,11] The lack of precise morphological control has not barred their commercial adoption. However, the omnipresent push toward device miniaturization has propelled inorganic semiconductor processing to achieve atomic-scale precision in device manufacturing. Forward-thinking in this field renders small molecules as attractive materials to service these demands in a way that

polymers cannot, making the distinctions between material types more pressing. Small molecules are monodisperse and have discrete molecular weights capable of well-defined crystallographic packing arrangements.

Though commonly utilized in polymer systems, self-doping is underdeveloped in small molecule-based materials. [12–16] While it has been applied to many semiconductors in the literature, the most common self-n-doped systems include fullerenes, naphthalene diimides, fluorenes, and perylene diimides.[17–21] Self-n-doping has rapidly risen to prominence, with recognized utility for solar energy conversion, solar energy harvesting, thermal energy harvesting, energy storage applications, and beyond.[22–28] This rise has coincided with the realization that the lack of systematic self-dopant structure-function relationships makes self-dopant design principles difficult to establish, and it has been acknowledged by the field that improved fundamental understandings are critical to organic electronics.[29] To address this knowledge gap, we developed a series of self-n-doped perylene diimides (PDIs) wherein structural features are independently investigated for their impact on physical properties as measured by a variety of spectroscopic observables. The high oscillator strengths and internal quantum efficiencies of PDIs make them one of the most heavily investigated organic dyes,[30] with self-n-doped PDIs as some of the best-performing derivatives.[31–36] In analyzing our series, we determine which structural features can dramatically enhance doping, promote dopant dealkylation or impart stability, influence solubility for improved processing, alter carrier mobility, and even direct morphological orientation. By analyzing each observable relative to each grouping, the impact of each structural feature can be disambiguated. This allows for the determination of explicit dopant design principles in view of specific desired properties, which will aid in more efficient materials design and tuning properties "on demand" in future organic electronic devices.

RESULTS AND DISCUSSION

Electronic doping. Chemical structures for the 16 self-n-doped PDIs in this series are shown in **Figure 1** (synthesis and structural data available in the supporting information). The general naming scheme for these compounds represents the degree of steric encumbrance (denoted as A-D), followed by the tether length (two or six methylene units, -CH_2-), and the counterion (*e.g.*, A2I, A2OH, etc.). The structures can be grouped in three ways. From left to right, the dopant structures become progressively more sterically encumbered (four groups of four compounds). The compounds can also be segmented by the specific counterion coordinated to the ammonium moieties (two groups of eight compounds), and grouped according to the length of the aliphatic hydrocarbon tether between the dopant and PDI (two groups of eight compounds). This series was designed to investigate the influence of dopant tether length, counterion selection, and steric encumbrance on a variety of observables, such as doping efficiency, structural stability, morphology, and carrier mobility.

It is worth noting that we anticipate there to be some tradeoff between the proximity of the ammonium substituent to the imide acceptor and its rotatability; both of which are important for doping. Closer proximity intuitively increases doping efficiency in accordance with Marcus theory. But for the ammonium anion to come into close proximity with the acceptor, it needs to be able to rotate about the axis of the methylene carbon for proper donor/acceptor orientation. A back of the envelope calculation puts the eclipsing strain above 8 kcal mol^{-1} for a 2-methylene tether and would be substantially higher for a 1-methylene tether. Additionally, cyclic aminals are unstable to acidic hydrolysis type conditions. Acyclic aminals are even more prone to hydrolysis and dissociation, leading to potential cleavage of the $(CH_2)_1$ linker. For these reasons we opted to pursue $(CH_2)_2$ and $(CH_2)_6$ -based linkers.
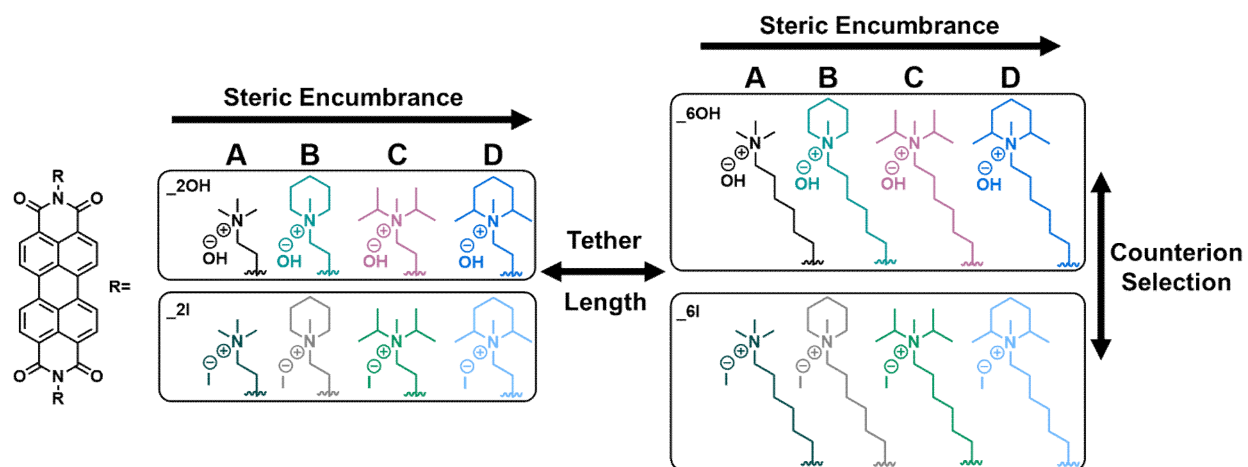
Figure 1. Dopant series tethered to the PDI backbone, which have three primary structural features: steric encumbrance, counterion selection, and tether length.

To elucidate the functional effects of these structural features, polarized near-edge X-ray absorption fine structure (NEXAFS) spectroscopy of the carbon K-edge was used to study the electronic structure of the 16 self-n-doped PDIs. In NEXAFS, the X-ray energy is resonant with the carbon K shell electronic transitions into unoccupied π^* and σ^* orbitals (280-300 eV),[37,38] and can thus be used to probe the density of unoccupied states for each compound in our series as a means of indirectly evaluating doping efficiency. **Figure 2** depicts exemplary NEXAFS spectra of D2OH and D2I collected at magic angle (54.7°), accompanied by a graphical representation of the different carbon environments in the π system. Spectra of the remaining compounds in the series are available in the supporting information (**Figures S1-S7**). The spectra can be generally subdivided into two regions; the π^* region where lower energy photons excite core electrons into states near the valence band, and the higher energy σ^* region of correspondingly greater photon energy. The individual resonances of the π^* region are color-coded and numbered to match that of the diagram depicting the different environments. As shown in **Figure 2A**, the discernable peaks

are assigned as follows: the resonance at 284.4 eV is assigned to core transitions from C1 and C2 into the lowest unoccupied molecular orbital (LUMO), the resonance at 285.1 eV is assigned to C3 and C4 into the LUMO, the resonance at 285.6 eV originates from C5 and C6 into LUMO+1 and LUMO+2,and the resonance at 288.5 eV is assigned to C7 into LUMO+5 and LUMO+7.[39–41] It is evident that the peak intensities of the LUMO transitions at 284.4 eV and 285.1 eV vary from sample to sample, but are more intense in those with iodide counterions than those with hydroxide counterions. **Figure 2B** depicts a generalized energy diagram of samples containing iodide (pink) and hydroxide (green) counterions. The K-shell to LUMO transition is limited in samples with hydroxide counterions due to the occupation of the LUMO that results from electronic doping. Thus, the intensity of the transitions at 284.4 eV and 285.1 eV are suppressed in samples with greater doping efficiency. It is emphasized that the only difference between these two systems is the counterion, and by simple visual inspection, the trend holds general for all PDIs in our series; those with iodide counterions tend to have much stronger LUMO resonances than those with hydroxide counterions. Therefore, we conclude that hydroxide counterions are stronger electron donors than iodide counterions. It should be noted that the intensities of the π^* resonances are polarization dependent, and therefore the absorbed intensity will change depending on the morphological orientation of the material relative to the sample substrate. Since we are comparing materials with differing morphologies (*vide infra*), differences in doping efficiency cannot be quantitatively determined. However, the angle-dependent NEXAFS spectra collected at 20°, 55°, and 90° still maintain this same general trend and we do not observe any striking changes in sample anisotropy, thus, we conclude that this trend is not morphologically driven (**Figure S8-S10**).
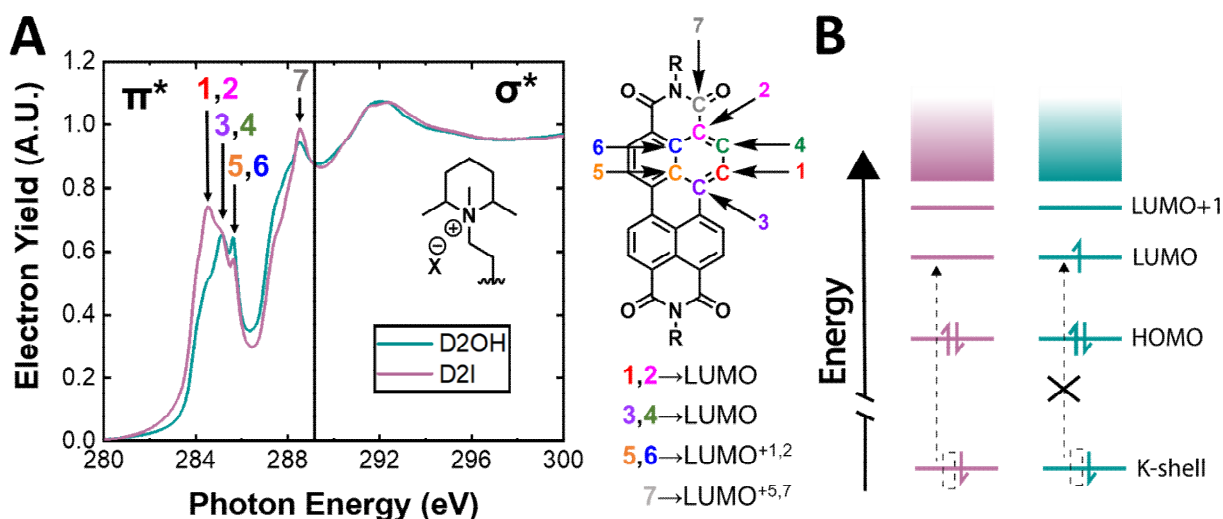
Figure 2. (A) NEXAFS spectra of D2OH and D2I accompanied by a diagram of numbered carbon atoms on the PDI core and corresponding transitions. **(B)** Energy level diagram depicting K-shell to LUMO transitions in iodide (pink) and hydroxide (green) samples. In samples containing the iodide counterions, the transition is allowed but disallowed in samples with hydroxide counterions as the corresponding LUMO is occupied.

A single electron reduction of the PDI molecule results in the formation of the paramagnetic PDI radical anion ($\mathbf{R^{\bullet-}}$). The concentration of $\mathbf{R^{\bullet-}}$ can be quantitatively measured using electron paramagnetic resonance (EPR) by constructing a standard sample calibration curve to determine the concentration of unpaired spins in the sample. It should be noted that the two-electron reduction of the PDI molecule forms a closed-shell dianion ($\mathbf{D^{\bullet\bullet2-}}$) which is not EPR active and could lead to an underestimation of doping when these species are present. **Figure 3** shows the spin concentration of each compound in the series. The spin concentrations range from $10^{20} - 10^{23}$ spins/mole upon self-doping the PDI molecules. We observe that the largest differentiator in doping efficiency between samples is counterion selection, which can increase

doping by more than 100x between samples with iodide and hydroxide counterions. Shorter tethers are also more efficient at doping than longer tethers by more than 10x. This trend follows chemical intuition; the donor and acceptor are more likely to be in close proximity to one another which raises the likelihood of a photoinitiated electron transfer event in accordance with Marcus theory. Surprisingly, steric encumbrance also enhances the doping efficiency of the anions by more than 10x. This finding contrasts with self-n-doped systems that employ sterically encumbered tertiary amines as dopants.[42] The divergence in trends is rationalized first by noting that the electron source in tertiary amines is a lone pair of electrons centered on nitrogen. Steric bulk limits the ability of the lone pair to spatially align with the imide acceptor moiety and initiate electron transfer. In contrast, when ammonium counterions are employed as dopants the anion itself acts as the electron donor.[43] In this case, steric encumbrance of the ammonium cation diminishes its ability to stabilize the anion by Coulombic interactions. Overall, the differences in doping density observed between compounds with shorter tether lengths and increased steric encumbrance are subtle in comparison to that of counterion selection. Thus, counterion selection can be used to dramatically alter the desired doping level while steric encumbrance and tether distance can be used for doping level refinements.

The doping efficiency of samples D2I and D6I do not follow the general trend that the rest of the molecules in our series follow as it is clear from **Figure 3** that steric encumbrance only improves doping efficiency in samples with iodide counterions. It should be noted that both D2I and D6I have roughly the same doping efficiency as A2I and A6I, so the incorporation of steric encumbrance does not have a detrimental effect. We note that the same trend depicted in **Figure 3** can also be observed in the low binding energy region of the ultraviolet photoelectron spectroscopy (UPS) data (*vide infra*) which shows that D2I and D6I exhibit the lowest built-in

potential shift of the HOMO to higher binding energy consistent with weak n-type doping. This phenomenon is not related to tether length since both the 2- and 6-methylene tethers show a decrease in efficiency. We can thus reasonably exclude Marcus theory considerations of conformational freedom and donor/acceptor proximity from our analysis. Since the same dimethyl piperidine structure enhances doping in compounds with hydroxide counterions, and steric encumbrance generally enhances doping efficiency in compounds with iodide counterions (B2I, B6I, C2I, and C6I), there is evidently a synergistic relationship between the steric profile and the iodide counterion that stifles the enhancive effect of steric encumbrance. This argument is further bolstered by the fact that D2I and D6I are the synthetic precursors to D2OH and D6OH, which exhibit the highest doping efficiencies in the series. Previous cyclic voltammetry experiments on A2I, B2I, C2I, and D2I reveal the first iodide oxidation wave ($3I^- \rightleftharpoons I_3^- + 2e^-$) shifts and becomes more electronegative in C2I and D2I, which we have attributed to the weak ion-pairing between ammonium and iodide making them more soluble and stronger electron donors.[44] As discussed later, X-ray photoelectron spectroscopy (XPS) measurements of the nitrogen 1s region also supports this assertion, as the binding energy of the NMe_3^+ region shifts to lower binding energy with increasing steric encumbrance (*vide infra*) due to decreased stability of nitrogen. This leads us to postulate that the high degree of instability and reactivity imparted to the iodide in D2I, taken together with a higher degree of solubility from weaker pairing with its counter cation, results in triiodide formation which quenches the enhancive doping effect.
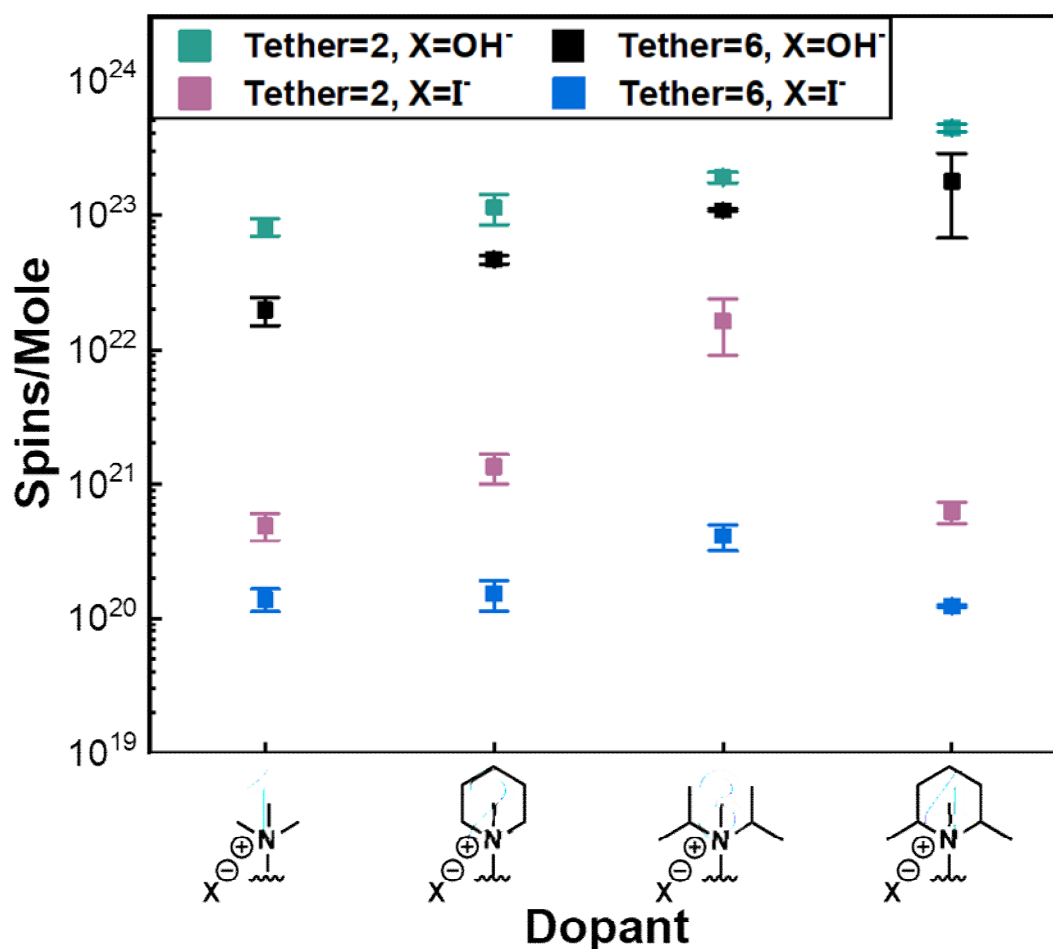
Figure 3. Quantitative EPR measurements for each compound in the series. Error bars were produced from triplicate sample measurements.

Numerous studies demonstrate enhanced doping levels in self-n-doped PDI thin films in response to thermal annealing.[45] However, it is unclear how dopant architecture impacts this process. The absorption spectra for thin films based on PDI molecules having hydroxide counterion derivatives are shown in **Figure 4**. The absorption spectra of neutral PDI monomers ^{0}**N** are characterized by an $S_0 \rightarrow S_1$ transition at ~560 nm (0-0) accompanied by Franck Condon vibronic transitions (0-1, 0-2, 0-3) of sequentially decreasing absorption intensity. Vibronic

coupling between adjacent PDI aggregates causes the intensities of these transitions to vary such that the 0-1 vibronic transition may become more intense than the primary 0-0 transition.[46,47] **R**$^{\bullet-}$ undergoes a $D_0 \rightarrow D_1$ transition starting at ~950 nm that is also accompanied by a complex vibronic structure down to ~650 nm.[48] Room temperature absorption spectra of the samples with two-methylene tethers are shown in **Figure 4A**. As with EPR, these samples exhibit a greater doping density than those with six-methylene tethers (**Figure 4B**) prior to annealing, as determined by the presence of **R**$^{\bullet-}$. Following thermal annealing at 120 °C for 1 h, the spectral intensity of the **R**$^{\bullet-}$ region rises due to solid-state doping, and the increase in **R**$^{\bullet-}$ is more pronounced in derivatives with six-methylene tethers than those with two-methylene tethers. Additionally, those with a greater degree of steric encumbrance generally exhibit a greater sensitivity to annealing. Interestingly, C2OH appears to be an exception and decreases in doping density upon annealing. This was affirmed to be the case after repeated scans. We hypothesize that upon annealing C2OH may be undergoing a structural and/or morphological arrangement that affects doping density as we do not believe the samples are being demethylated upon annealing as per our UPS studies. Additionally, the peak ratios of the $S_0 \rightarrow S_1$ peaks also change in response to annealing since PDIs are crystallochromic materials, and even modest crystallographic displacements can give rise to substantial changes in the vibronic structure.[49] These changes indicate that thermal annealing alters the morphology of the PDIs. In contrast, the absorption spectra of samples with iodide counterions (**Figures S11-S12**) are predominantly neutral both before and after thermal annealing and exhibit comparable changes in vibronic structure. Samples with iodide counterions and six-methylene tethers exhibit small but noticeable increases in the absorption intensity of the **R**$^{\bullet-}$ region after annealing. Thus, in both the ammonium hydroxide and ammonium iodide doped samples, those with longer tethers are more sensitive to annealing. Previous Jablonski and energy level diagrams

for these self-doped PDI molecules obtained via combination of steady-state and transient absorption spectroscopy studies suggest that different electron transfer pathways can be accessed depending on the excitation wavelength. For example, samples excited at lower energies bleaches the $S_0 \rightarrow S_1$ transition of **N** accompanied by stimulated emission and a $S_1 \rightarrow S_n$ absorption transient of ^{1}[**N**]* while samples excited at higher energies bleaches the $D_0 \rightarrow D_1$ transition of **R**$^{\bullet-}$ and is accompanied by the transient absorption of the ground-state excitation.[44]
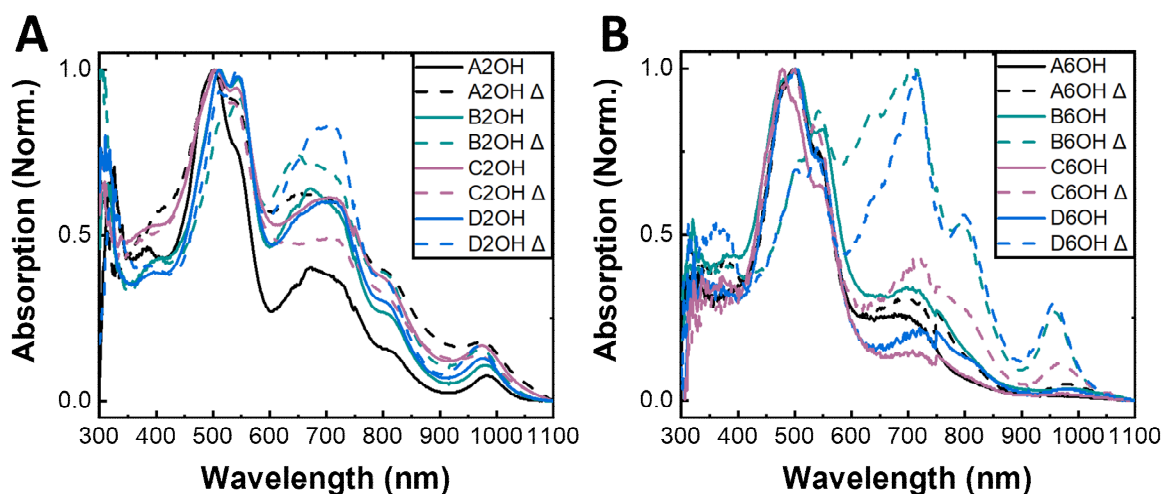
Figure 4. Absorption spectra of self-n-doped PDIs with hydroxide counterions before and after thermal annealing (Δ). **(A)** The family of compounds with two-methylene tethers and **(B)** six-methylene tethers.

Doping alters the work function (Φ) of semiconductors and provides a fingerprint of electron injection into PDI from the counterions. Changes in Φ were measured by performing UPS measurements to understand how counterion selection impacts doping. **Figure 5** depicts a set of UPS spectra for compounds containing a two-methylene tether. The secondary electron cutoffs (E_{cutoff}) in **Figure 5A** all shift to higher binding energy in samples with hydroxide counterions compared to a shift to lower binding energy for samples with iodide counterions, corresponding to a decrease in Φ according to equation 1:[50]

$$\Phi = h\nu - E_{cutoff} \qquad (1)$$

Where $h\nu$ is the He I energy of 21.2 eV. Calibration of the UPS measurements was conducted via the acquisition of the UPS spectrum of a silver reference. **Table 1** presents the Φ values for each sample. The Φ values decrease by ~0.2 eV when iodide is substituted for hydroxide. Differences in Φ are slightly more pronounced in samples with six-methylene length tethers when swapping iodide for hydroxide counterions. The low binding energy regions displayed in **Figure 5B** show a built-in potential shift of the HOMO level to higher binding energies in samples with hydroxide counterions compared to that observed for samples with iodide counterions, which is consistent with systems exhibiting stronger n-type doping.[51,52] The UPS spectra obtained for each compound before and after annealing at 120°C for 1 h are shown in **Figures S13-S28**. In some cases, annealing causes Φ to shift up to +0.1 eV accompanied by an increase in valence and deep state filling. This is most pronounced in samples that exhibit thermal degradation likely due to a combination of decomposition and doping.

**Table 1.** Work function values for each self-n-doped PDI in the series.

Sample ID	Φ (eV)	Sample ID	Φ (eV)	Sample ID	Φ (eV)	Sample ID	Φ (eV)
A2I	4.0	A2OH	3.8	A6I	3.8	A6OH	3.7
B2I	3.9	B2OH	3.9	B6I	3.8	B6OH	3.6
C2I	3.9	C2OH	3.8	C6I	3.9	C6OH	3.6
D2I	3.9	D2OH	3.8	D6I	4.0	D6OH	3.6
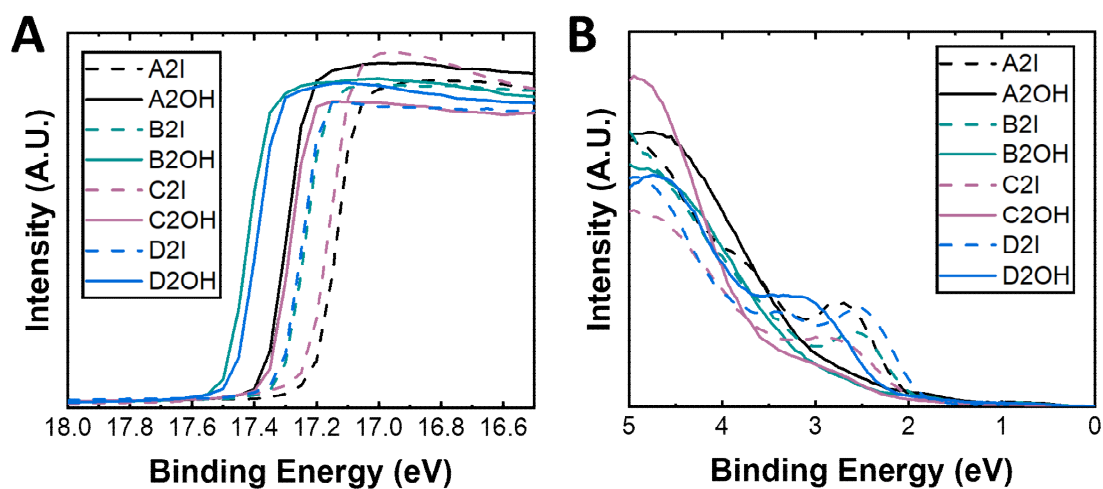
Figure 5. **(A)** UPS spectra of the family of compounds self-n-doped PDIs with two-methylene tethers in the high binding energy region (secondary electron cutoff edge) and **(B)** low binding energy region.

Structural stability. It was demonstrated in the previous section that thermal annealing promotes doping in samples with hydroxide counterions. In some instances, amine and ammonium anion dopants have been shown to promote dealkylation or demethylation of the amino moiety in response to photoirradiation or thermal annealing.[53,54] X-ray photoelectron spectroscopy (XPS) was used to evaluate the stability of the dopants in our series, which can then be correlated to our absorption data. **Figure 6** shows the XPS spectra of the N 1s region for each compound in the series both before and after thermal annealing (I 3d, O 1s, and C 1s regions available in **Figures S30-S45**). Peaks at 402 eV can be assigned to the quaternary ammonium nitrogen atoms, while those at 400 eV and 398.5 eV are assigned to the imide nitrogen and tertiary amine nitrogen atoms, respectively.[55] Thus, the conversion from the quaternary ammonium to the tertiary amine can be qualitatively evaluated with XPS. Of the 16 compounds measured, six showed signs of dealkylation (all six samples with hydroxide counterions, i.e., A2OH, B2OH, C2OH, D2OH, A6OH and B6OH), presumed to be demethylation in all cases. Some trends can be noted in how the various structural parameters influence stability. First, counterion selection is the primary determinant of stability. Additionally, the compounds with two-methylene length tethers degraded and were less stable overall when compared to those with a six-methylene tether, which prevented the degradation of C6I and D6OH. Additionally, the degree of degradation in the samples with six-methylene tethers is less than that of their two-methylene tether variants. We attribute the abundance of the tertiary amine in these samples to photodegradation during sample preparation from ambient light in the counterion exchange resin, and unreacted tertiary amine during quaternization.
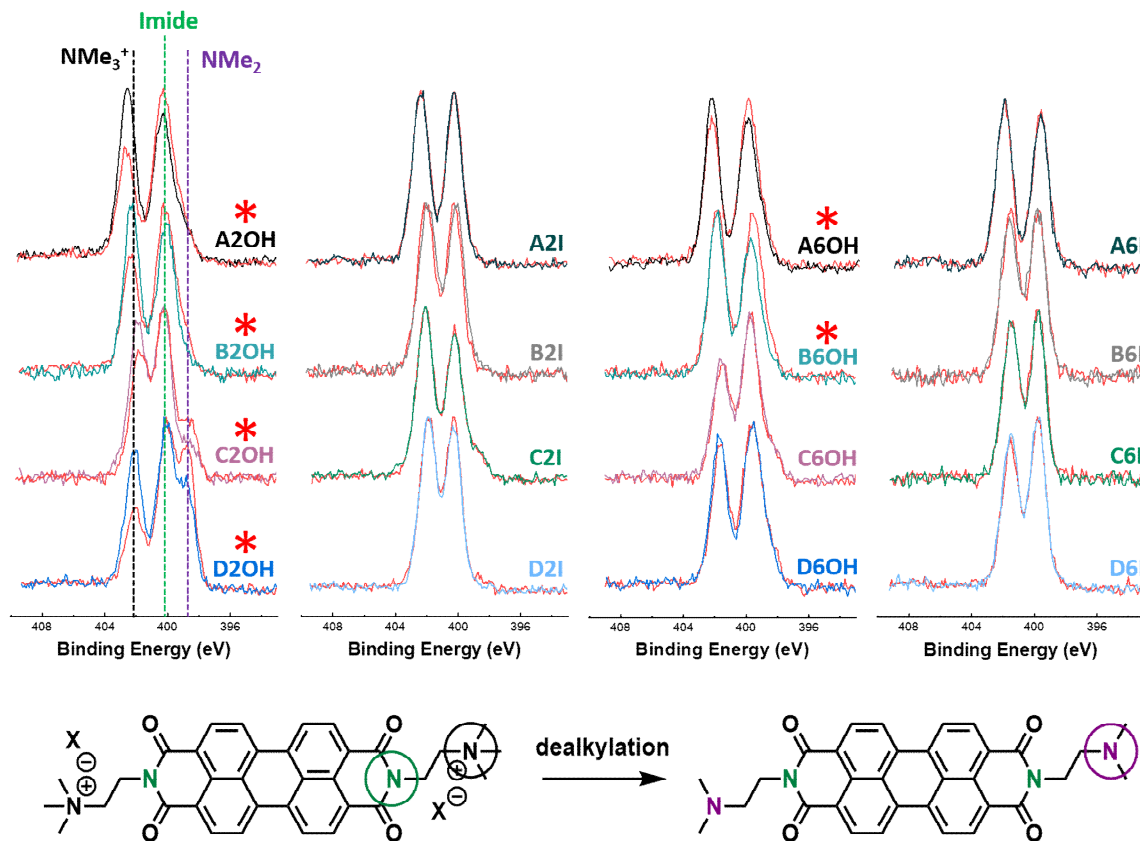
Figure 6. XPS spectra of the N 1s region for each compound in the series before (colored) and after (red) annealing at 120 °C for 1 h. Compounds that show signs of demethylation are marked with a red asterisk. Peaks at 402 eV correspond to the ammonium nitrogen, peaks at 400 eV correspond to the imide nitrogen, and peaks at 398.5 eV correspond to the demethylated tertiary amine.

The mechanism by which thermal annealing enhances doping has been a topic of debate. The Gibbs free energy barrier for charge transfer between the latent electrons of amine-based dopants and the LUMO of PDI is sufficiently large to prevent spontaneous electron transfer. It is known that doping can proceed via a photoinitiated transfer mechanism wherein the neutral ground state ^{0}N of PDI is photoexcited to the singlet state ^{1}[N]*, a strong oxidant (+1.97 V vs. SCE), that

is then reductively quenched by the dopant to yield the radical anion $\mathbf{R^{\bullet-}}$.[44,56] However, direct thermal excitation (~25-40 meV) is insufficient to overcome the energy barrier of charge transfer (ΔG_{CT} ~1.4 eV), and it was proposed by Russ et al. that thermal annealing promotes demethylation of the quaternary ammonium to yield the tertiary amine which is then able to dope the PDI backbone through a photoinitiated electron transfer process.[55] However, the absorption spectra of C6OH and D6OH in **Figure 4B** show dramatic increases in $\mathbf{R^{\bullet-}}$ in response to annealing, yet these dopants do not demethylate. Additionally, the view that quaternary ammonium dopants must first demethylate to a tertiary amine prior to electron donation from a lone pair is not supported by our UPS results, nor the increase in doping observed in sterically encumbered dopants. Support for this hypothesis would require the doping efficiency of sterically encumbered quaternary ammonium dopants to decrease, yet the opposite trend is observed. The hypothesis is also not supported by related reports which unambiguously identify counterions as electron donors.[43] When structural degradation has been identified in self-n-doped systems, it occurs after the dopant has already donated an electron to the acceptor in a downstream process.[54] It is therefore unclear how a sequence of degradation reactions would result in a greater density of unpaired electrons by a factor of three or more. Instead, we have found that doping is strongly dependent upon the solvent environment of the materials. **Figure 7** depicts absorption spectra of A2I in 10 µM solutions of water and DMF after several days of ambient light exposure. Both solutions were prepared the same day and stored in the same manner. We observe that the presence of water suppresses the formation of $\mathbf{R^{\bullet-}}$. A similar observation is noted by acquiring the absorption spectra for A2OH in 10 µM solutions of water and DMF (**Figure S29**). Wang et al. also observed solvent-dependent doping suppression in self-n-doped PDI thin films following thermal annealing.[57] This leads us to propose that dealkylation is merely a phenomenological feature of certain structural motifs and is

not primarily responsible for thermally enhanced doping. Instead, thermal annealing removes residual solvents like water from the material, which quenches charge transfer, and allows the photoinitiated electron transfer process to occur. Additionally, electron transfer depends on the geometries of the donor relative to the acceptor in accordance with Marcus theory. In the solid-state, the morphology is well defined compared to other matter phases, and the probability of reductive quenching decreases substantially. Thermal annealing may also allow for some degree of molecular reorganization by increasing thermal motions within the van der Waals lattice, which would increase the likelihood of reductive quenching.
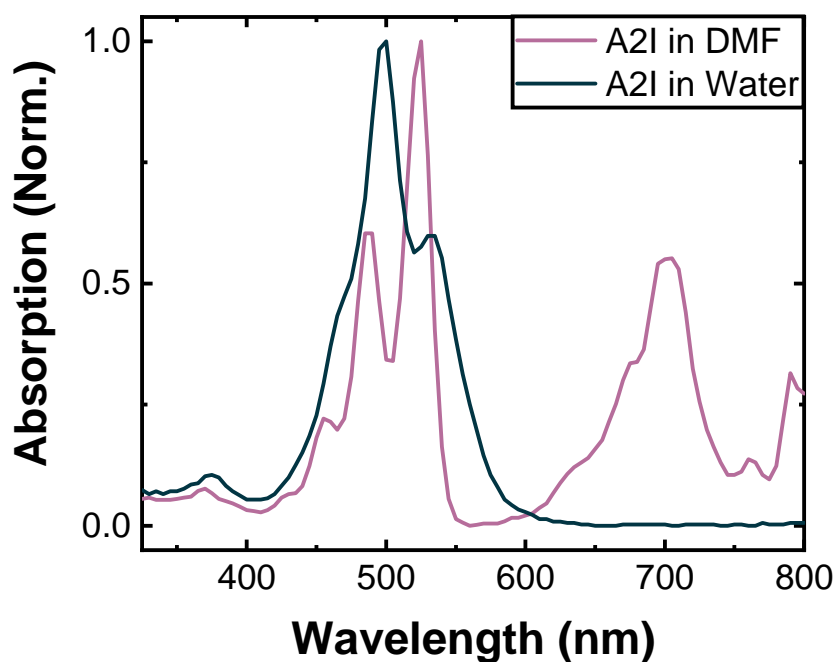

Figure 7. Absorption spectra of 10 µM solutions of A2I after several days of exposure to ambient light.

Morphology. The different dopant motifs alter the solubility properties of the materials. While samples with hydroxide counterions show good solubility in water, the solubility decreases with increasing steric encumbrance. Samples with iodide counterions are modestly soluble in water and were instead spin-coated from DMF solutions. Atomic force microscopy (AFM) was used to evaluate the quality of the thin films produced via spin-coating. AFM images of each sample are available in the supporting information (**Figures S46-S53**). Overall, spin coating yields continuous and smooth thin films with average surface roughness values ranging from 35.2 nm for A6I to 0.23 nm for D6I. In all samples with iodide counterions, the solubility in DMF is improved by steric encumbrance and yields smoother films.

The morphological orientation of the π system on the PDI core can substantially impact the isotropic and anisotropic charge transport properties of the material. We performed grazing incidence wide-angle X-ray scattering (GIWAXS) measurements to probe the morphological orientation of the PDIs relative to the sample substrate. **Figures 8A-B** present GIWAXS images for A2OH and A2I thin films deposited onto glass substrates, respectively. Given that the samples are polycrystalline and the diffraction patterns show a limited number of scattering features, crystal structure and Miller indexes assignments are challenging. However, it is evident that the film morphologies and crystallite orientations are different upon changing the counterions. Interchromophore π—π stacking in A2OH is oriented along the q_{xy} with a chromophore spacing of ~1.87 Å^{-1}. The orientation of π—π stacking along the q_{xy} is indicative of edge-on orientation of the PDI cores and lamella stacking in the q_z plane. In contrast, π—π stacking in A2I is oriented along the q_z plane indicative of face-on stacking. Interestingly, all samples with two-methylene tethers exhibit this same morphological trend (**Figures S54-S57**); hydroxide counterions direct sample orientation edge-on while iodide counterions exhibit loss of coherent π—π stacking. This

trend disappears in samples with six-methylene tethers (**Figures S58-S61**). However, samples with hydroxide counterions do exhibit a greater number of Miller index reflections than the iodide samples on average.
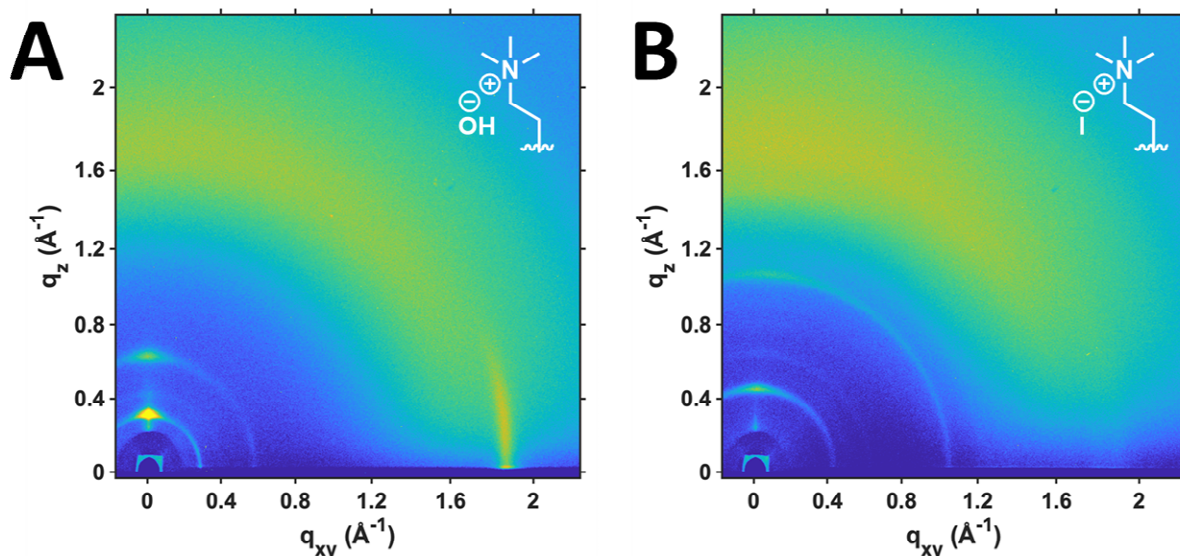
Figure 8. GIWAXS images of **(A)** A2OH and **(B)** A2I thin films.

To investigate the impact of thermal annealing on morphological order, samples with hydroxide counterions were analyzed using in-situ GIWAXS. Samples with hydroxide counterions were selected due to their strong degree of preferential orientation observed with standard GIWAXS. Briefly, a GIWAXS image is collected at a specific location on the thin film, heated to 120 °C for 1 h, and then another GIWAXS image is collected in-situ. **Figure 9** depicts the room temperature and in-situ GIWAXS for a D2OH thin film. At room temperature, D2OH exhibits several sharp Miller index reflections that are well oriented along several φ azimuthal angles and has a strong degree of edge-on π—π stacking, as shown in **Figure 9A**. The in-situ GIWAXS image of D2OH collected at 120 °C is shown in **Figure 9B**. To best interpret the changes that occur upon

annealing, horizontal and vertical intensity linecuts are presented in **Figure 9C-D**. The horizontal linecuts show that annealing causes the π—π stacking distance to increase slightly (decrease in q_r Å^{-1}). At the same time, the vertical linecut shows that the Miller index reflection at 0.43 Å^{-1} shifts to 0.46 Å^{-1} upon annealing. The other Miller indices observed along φ also exhibit this shift, which is attributed to an overall shrinkage in the spacing between crystallite grains due to a thermally expanded van der Waals lattice. In-situ GIWAXS images of the remaining samples, as well as the horizontal and vertical linecuts, are presented in **Figures S62-S75**. In the cases of C2OH, A6OH, and B6OH (**Figure S66**, **S68**, and **S70**), annealing decreases the azimuthal distributions of the reflections at 0.62 Å^{-1}, 0.81 Å^{-1}, and 0.68 Å^{-1} for better orientation along $\varphi = 90°$. A key discernable structural feature among the compounds is that those with two-methylene tethers exhibit an increase in π stacking distance and a decrease in crystallite grain boundaries.
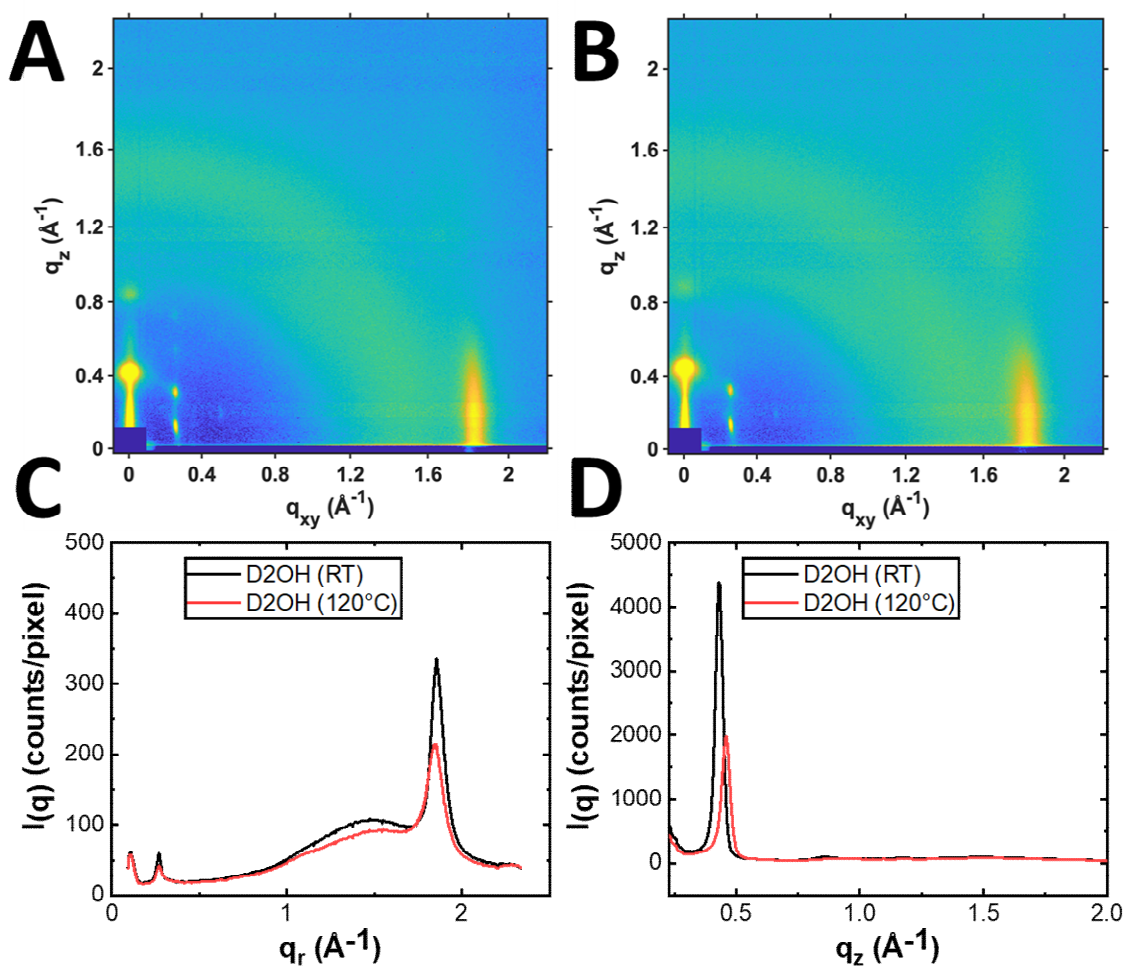
Figure 9. **(A)** GIWAXS image of D2OH collected at room temperature. **(B)** in-situ GIWAXS image after annealing at 120°C for 1 h. **(C)** Overlaid horizontal (q_r) linecuts of both images. **(D)** Vertical (q_z) linecuts of both images.

Carrier mobility. Carrier mobility is an important parameter in semiconductors because it describes how quickly carriers move throughout the material, for a given electric field. The electrical conductivity is a product of the carrier mobility and carrier concentration in the sample, which for an electron transporting material is given by equation 2:[58]

$$\sigma = ne\mu \qquad\qquad (2)$$

where σ is the electrical conductivity (Scm^{-1}), n is the carrier concentration(cm^{-3}) , e is the magnitude of the elementary unit of charge (C), and μ is the carrier mobility mobility (cm^{2}V^{-1}s^{-1}). It is known that the electrical conductivity in self-n-doped PDIs increases by several orders of magnitude after annealing,[45] yet it is unknown whether this increase is strictly due to an increase in carrier concentration, or a combination of this with an increase in carrier mobility due to improved morphological ordering. Carrier mobility can be challenging to measure unambiguously. Common strategies, such as with thin film transistor measurements, while well established,[59] are highly dependent on device optimization and processing protocols.[60,61] For this reason, significant variations in field-effect mobility can be reported for identical semiconductors,[62] depending on how the device was fabricated. Deconvoluting device fabrication and testing inconsistencies from extracted mobility parameters makes direct sample comparisons in large sample sets problematic. Time-resolved microwave conductivity (TRMC) is a contactless method that can be useful in evaluating carrier mobility in samples that are challenging to measure by traditional means.[63] TRMC situates samples inside a microwave resonator cavity oriented with the plane of the sample parallel to electric field component of the standing microwaves in the cavity. Samples are then irradiated with a short 532 nm laser pulse which excites neutral PDI ^{0}**N** to ^{1}**[N]***. The electric field in the cavity causes the carriers to move throughout the material, and the photoconductance (ΔG)

is measured by detecting changes in the intensity of the reflected microwaves in the cavity. The photoconductance is a function of carrier lifetime and decays to zero as carriers recombine. The maximum photoconductance measured (ΔG_{max}) can be used to determine the TRMC figure of merit $\phi\Sigma\mu$, as given by equation 3:[63]

$$\phi\Sigma\mu = \phi(\mu_e + \mu_h) \qquad (3)$$

ϕ is the fraction of generated electron-hole pairs per photon, μ_e is the average electron mobility and μ_h is the average hole mobility. ΔG_{max} is measured in the samples at multiple fluences and fit to obtain $\phi\Sigma\mu$.[64] Fluence-dependent data and fits are shown in **Figures S76-S107**. While ϕ is normally lower than unity in organic semiconductors,[65] it is unlikely to vary significantly between the materials studied here. Similarly, although $\phi\Sigma\mu$ does contain contributions from both holes and electrons, for systems known to be dominated by electron transport such as PDIs, it is reasonable to interpret $\phi\Sigma\mu$ in an analogous manner to electron mobility. It is worth noting that while TRMC uses a laser pulse to excite **⁰N** in order to measure the mobility properties of **¹[N]***, **R•⁻** states are present in our materials at abundances evaluated by quantitative EPR. Additionally, **R•⁻** increases in abundance when samples are annealed, leading to a lower abundance of excitable **⁰N** in the thin films which may introduce error into the measurements. However, sample to sample comparisons are informative.

The TRMC figure of merit values are plotted in **Figure 10** for all compounds before and after thermal annealing (tabulated values in **Table S1**). All the samples exhibit comparable carrier mobility values except for A2I, which is considerably higher than the others (0.2 cm^2 V^{-1} S^{-1}), and quite high compared to other PDIs measured by TRMC.[66] It should be noted that are measuring photoconductance with TRMC and not electrical conductivity. The higher carrier mobility

observed for A2I can be explained by the fact that this molecule is a strong photoabsorber compared to the other self-doped materials which in turn will yield a higher photoconductance. Additionally, some subtle trends are discernable among the samples. First, sterically encumbered samples tend to be more resistant to changes in carrier mobility in response to annealing. Additionally, with the exception of A2OH, samples with hydroxide counterions either remained the same or increased in mobility following annealing, which we attribute to grain boundary shrinking observed in the in-situ GIWAXS studies at elevated temperatures. Additionally, despite the diverse range of morphologies present in these materials, the mobility values are in good agreement with one another. It is interesting to note that annealing decreases mobility in some samples, which highlights the extent of unknown morphological parameters that must be evaluated on a deeper level to understand these changes. It should be noted that unlike electrical measurements, where charges must travel ~µm to be extracted and hence detectable, TRMC is a local probe, so the relationship between mobility and morphology can be distinct.[67] More importantly, these results provide direct evidence that changes in carrier mobility in self-n-doped PDIs are relatively unsubstantial and cannot account for the large increases in electrical conductivity typically observed in these materials following annealing. This result also provides indirect evidence that doping primarily generates free carriers, though future work in this area could establish the branching ratio between bound states and free carriers. We emphasize the importance of dopant structural design in maximizing doping efficiency to improve performance.
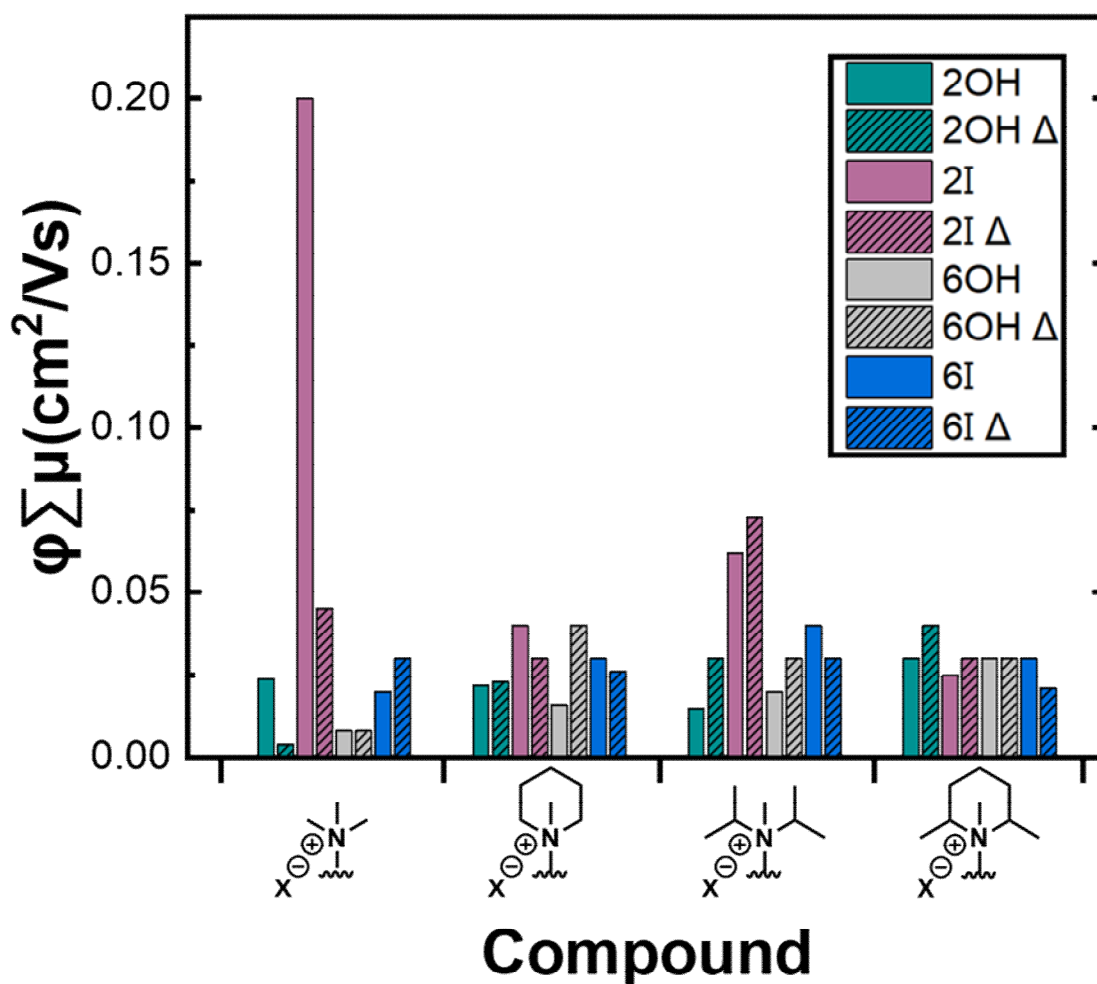
Figure 10. TRMC figure of merit ($\phi\Sigma\mu$) summary plot. Unannealed samples are solid colors and annealed samples are grated. Samples are grouped according to their degree of steric encumbrance.

In view of the doping, stability, morphology and mobility features studied both at room temperature and after thermal annealing, we are able to draw explicit structure-function relationships in self-n-doped materials. **Figure 11** summarizes the structure-function relationships that were developed for self-n-doped PDIs. Hydroxide counterions act as potent electronic dopants that are sensitive to thermal activation and improve morphological ordering but tend to modestly

decrease carrier mobility and are prone to dealkylation. Conversely, iodide counterions are weaker Lewis bases and relatively insensitive to thermal annealing but are relatively stable and promote good carrier mobilities. Two-methylene tethers between the ammonium moiety and the PDI core improve the doping efficiency and morphology compared to those with six-methylene tethers but are less sensitive to thermal activation and are more prone to demethylation. Steric encumbrance is the only structural parameter identified that does not demonstrate any explicit drawbacks. The doping efficiency is increased when sterics are included as a structural parameter, and it also modestly protects the materials from dealkylation.
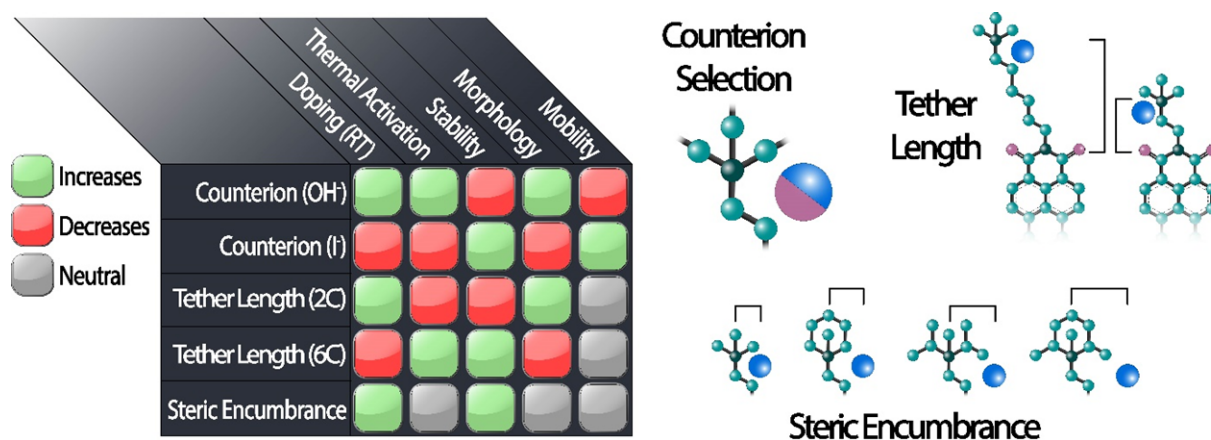
Figure 11. Summary of how the various dopant structural parameters influence the function and morphology of PDIs. Dopant structural features that increase or improve a given function are shown in green while those that decrease or hinder the functionality are shown in red. Those with no discernable effect are shown in grey.

CONCLUSION

A series of 16 self-n-doped perylene diimides (PDI) were carefully selected to generate self-n-dopant design principles applicable to organic electronics by investigating the influence of counterion selection, tether length, and steric encumbrance on doping, stability, morphology, and carrier mobility. Counterion selection is found to be the most important parameter when designing self-n-doped systems, which can increase doping by more than 100-fold, promote sample degradation or impart structural stability, alter solubility for improved processing, influence carrier mobility, and even direct morphological orientation in structurally diverse systems. The tether length between the ammonium moiety and the PDI core influences doping efficiency, with two-methylene tethers being at least 10-fold more effective dopants than those with six-methylene tethers due to the increased proximity of the donor and acceptor groups. Six-methylene tethers also tend to impart some degree of stability to the dopants but tend to adopt more amorphous morphologies than those with short tethers. Steric encumbrance of the ammonium cation enhances the doping efficiency of anions by Coulombic destabilization and imparts stability. In addition to these structure-function relationships, we identify examples of structurally stable self-n-dopants that do not degrade in response to thermal annealing, yet they exhibit strong n-type doping. Moreover, the presence of water is found to directly inhibit doping, leading us to conclude that structural degradation is merely a phenomenological feature of certain structural motifs that is independent of the self-n-doping process. Thermal annealing can enhance doping by removing moisture from the thin films. Thermal annealing also tends to shrink grain boundaries in some of the samples which improves carrier mobility. Carrier mobility remains relatively consistent among PDI samples, which implicates doping as the primary modulator of electrical conductivity in response to thermal annealing. We anticipate these findings to be of broad significance with the

advent of self-n-doped small molecule semiconductors and potentially adapted to improve properties in polymer-based materials as well.

ASSOCIATED CONTENT

Supporting Information

The Supporting Information is available free of charge at https://pubs.acs.org.

The supporting information contains relevant information related to synthesis and structural data, thin film fabrication, NEXAFS, EPR, absorption, UPS, XPS, AFM, GIWAXS, in-situ GIWAXS, and TRMC.

AUTHOR INFORMATION

Corresponding author

*Luisa Whittaker-Brooks –Department of Chemistry, University of Utah, Salt Lake City, Utah 84112, United States; ORCID: http://orcid.org/0000-0002-1130-1306; Email: luisa.whittaker@utah.edu

Authors

Daniel Powell –Department of Chemistry, University of Utah, Salt Lake City, Utah 84112, United States; ORCID: http://orcid.org/0000-0002-5893-0695

Xueqiao Zhang – School of Electrical Engineering and Computer Science, Oregon State University, Corvallis, OR 97331, United States

Chideraa I. Nwachukwu –Department of Chemistry, University of Utah, Salt Lake City, Utah 84112, United States; ORCID: http://orcid.org/0000-0002-9143-3228

Edwin J. Miller –Department of Chemistry, University of Utah, Salt Lake City, Utah 84112, United States

Kameron R. Hansen –Department of Chemistry, University of Utah, Salt Lake City, Utah 84112, United States; ORCID: http://orcid.org/0000-0001-9037-8135

Laura Flannery –Department of Chemistry, University of Utah, Salt Lake City, Utah 84112, United States; ORCID: http://orcid.org/0000-0002-6118-4080

Jonathan Ogle –Department of Chemistry, University of Utah, Salt Lake City, Utah 84112, United States; ORCID: http://orcid.org/0000-0003-3166-8954

Alex Berzansky –Department of Chemistry, University of Utah, Salt Lake City, Utah 84112, United States; ORCID: http://orcid.org/0000-0002-8556-3317

John G. Labram – School of Electrical Engineering and Computer Science, Oregon State University, Corvallis, OR 97331, United States; ORCID: http://orcid.org/0000-0001-6562-9895

Andrew G. Roberts –Department of Chemistry, University of Utah, Salt Lake City, Utah 84112, United States; ORCID: http://orcid.org/0000-0002-2221-534X

Author contributions

This manuscript was written through the contributions of all authors. All authors have given approval to the final version of the manuscript.

Notes

The authors declare no competing financial interest.

ACKNOWLEDGEMENTS

REFERENCES

(1)   *The Nobel Prize in Chemistry 2000 - Advanced information - NobelPrize.org.* https://www.nobelprize.org/prizes/chemistry/2000/advanced-information/ (accessed 2022-07-12).

(2)   Shirakawa, H.; Louis, E. J.; MacDiarmid, A. G.; Chiang, C. H.; Heeger, A. J. Synthesis of Electrically Conducting Organic Polymers : Halogen Derivatives of Polyacetylene, $(CH)_x$. *J. Chem. Soc., Chem. Commun.*, **1977**, 578-580.

(3)   Patil, A. O.; Ikenoue, Y.; Basescu, N.; Colaneri, N.; Chen, J.; Wudl, F.; Heeger, A. J. Self-Doped Conducting Polymers. *Synth. Met.* **1987**, *20*, 151–159.

(4)   Havinga, E. E.; Ten Hoeve, W.; Meijer, E. W.; Wynberg, H. Water-Soluble Self-Doped 3-Substituted Polypyrroles. *Chem. Mater.* **1989**, *1*, 650–659.

(5)   Jacobs, I. E.; Aasen, E. W.; Oliveira, J. L.; Fonseca, T. N.; Roehling, J. D.; Li, J.; Zhang, G.; Augustine, M. P.; Mascal, M.; Moulé, A. J. Comparison of Solution-Mixed and Sequentially Processed P3HT:F4TCNQ Films: Effect of Doping-Induced Aggregation on Film Morphology. *J. Mater. Chem. C* **2016**, *4*, 3454–3466.

(6)   Duong, D. T.; Wang, C.; Antono, E.; Toney, M. F.; Salleo, A. The Chemical and Structural Origin of Efficient P-Type Doping in P3HT. *Org. Electron.* **2013**, *14*, 1330–1336.

(7)   Freund, M. S.; Deore, B. A. Self-Doped Conducting Polymers; Chapter 5, Wiley, 2007.

(8)   Mishra, A.; Bäuerle, P. Small Molecule Organic Semiconductors on the Move: Promises for Future Solar Energy Technology. *Angew. Chem. Int. Ed.* **2012**, 51, 2020–2067.

(9)   Gu, Y.; Zhao, J.; Johnson, J. A. Polymer Networks: From Plastics and Gels to Porous Frameworks. *Angew. Chem. Int. Ed.* **2020**, 59, 5022–5049.

(10)   Dongmin Kang, S.; Jeffrey Snyder, G. Charge-Transport Model for Conducting Polymers. *Nat. Mater.* **2016**, 16, 252–257.

(11)   Noriega, R.; Rivnay, J.; Vandewal, K.; Koch, F. P. V.; Stingelin, N.; Smith, P.; Toney, M. F.; Salleo, A. A General Relationship between Disorder, Aggregation and Charge Transport in Conjugated Polymers. *Nat. Mater.* **2013**, 12, 1038–1044.

(12)   Wang, S.; Li, Z.; Xu, X.; Zhang, M.; Zhang, G.; Li, Y.; Peng, Q. Self-Doping Small Molecular Conjugated Electrolytes Enabled by n-Type Side Chains for Highly Efficient Non-Fullerene Polymer Solar Cells. *J. Mater. Chem. A* **2018**, 6, 22503–22507.

(13)   Lee, B. H.; Jung, I. H.; Woo, H. Y.; Shim, H. K.; Kim, G.; Lee, K. Multi-Charged Conjugated Polyelectrolytes as a Versatile Work Function Modifier for Organic Electronic Devices. *Adv. Funct. Mater.* **2014**, 24, 1100–1108.

(14)   Tang, H.; Liu, Z.; Tang, Y.; Du, Z.; Liang, Y.; Hu, Z.; Zhang, K.; Huang, F.; Cao, Y. Organic Diradicals Enabled N-Type Self-Doped Conjugated Polyelectrolyte with High Transparency and Enhanced Conductivity. *Giant* **2021**, 6, 100053.

(15)   Zhao, C.; Tang, C. G.; Seah, Z. L.; Koh, Q. M.; Chua, L. L.; Png, R. Q.; Ho, P. K. H. Improving Organic Photovoltaic Cells by Forcing Electrode Work Function Well beyond Onset of Ohmic Transition. *Nat. Commun.* **2021**, 12, 1-9.

(16)   Tang, C. G.; Ang, M. C. Y.; Choo, K.-K.; Keerthi, V.; Tan, J.-K.; Syafiqah, M. N.; Kugler, T.; Burroughes, J. H.; Png, R.-Q.; Chua, L.-L.; Ho, P. K. H. Doped Polymer Semiconductors with Ultrahigh and Ultralow Work Functions for Ohmic Contacts. *Nature* **2016**, 539, 536–540.

(17)   Keshri, S. K.; Mandal, K.; Kumar, Y.; Yadav, D.; Mukhopadhyay, P. Naphthalenediimides with High Fluorescence Quantum Yield: Bright-Red, Stable, and Responsive Fluorescent Dyes. *Chem. Eur. J.* **2021**, 27, 6954–6962.

(18)   Li, C. Z.; Chueh, C. C.; Yip, H. L.; Ding, F.; Li, X.; Jen, A. K. Y. Solution-Processible Highly Conducting Fullerenes. *Adv. Mater.* **2013**, 25, 2457–2461.

(19)   O'Malley, K. M.; Li, C. Z.; Yip, H. L.; Jen, A. K. Y. Enhanced Open-Circuit Voltage in High Performance Polymer/Fullerene Bulk-Heterojunction Solar Cells by Cathode Modification with a C_{60} Surfactant. *Adv. Energy Mater.* **2012**, 2, 82–86.

(20)   Chen, W.; Jiao, W.; Li, D.; Sun, X.; Guo, X.; Lei, M.; Wang, Q.; Li, Y. Cross Self-n-Doping and Electron Transfer Model in a Stable and Highly Conductive Fullerene Ammonium Iodide: A Promising Cathode Interlayer in Organic Solar Cells. *Chem. Mater.* **2016**, 28, 1227–1235.

(21)   Jiao, W.; Ma, D.; Lv, M.; Chen, W.; Wang, H.; Zhu, J.; Lei, M.; Chen, X. Self N-Doped [6,6]-Phenyl-C61-Butyric Acid 2-((2-(Trimethylammonium)Ethyl)- (Dimethyl)Ammonium) Ethyl Ester Diiodides as a Cathode Interlayer for Inverted Polymer Solar Cells. *J. Mater. Chem. A* **2014**, 2, 14720–14728.

(22)   Kang, Q.; Ye, L.; Xu, B.; An, C.; Stuard, S. J.; Zhang, S.; Yao, H.; Ade, H.; Hou, J. A Printable Organic Cathode Interlayer Enables over 13% Efficiency for 1-cm^2 Organic Solar Cells. *Joule* **2019**, 3, 227–239.

(23)   Tang, C. G.; Ang, M. C. Y.; Choo, K. K.; Keerthi, V.; Tan, J. K.; Syafiqah, M. N.; Kugler, T.; Burroughes, J. H.; Png, R. Q.; Chua, L. L.; Ho, P. K. H. Doped Polymer Semiconductors with Ultrahigh and Ultralow Work Functions for Ohmic Contacts. *Nature* **2016**, 539, 536–540.

(24)   Sun, X.; Chen, W.; Liang, L.; Hu, W.; Wang, H.; Pang, Z.; Ye, Y.; Hu, X.; Wang, Q.; Kong, X.; Jin, Y.; Lei, M. Construction of Electron Transfer Network by Self-Assembly of Self-n-Doped Fullerene Ammonium Iodide. *Chem. Mater.* **2016**, 28, 8726–8731.

(25)   Jia, J.; Fan, B.; Xiao, M.; Jia, T.; Jin, Y.; Li, Y.; Huang, F.; Cao, Y. N-Type Self-Doped Water/Alcohol-Soluble Conjugated Polymers with Tailored Energy Levels for High-Performance Polymer Solar Cells. Macromolecules **2018**, 51, 2195–2202.

(26)   Gao, C.; Liu, Y.; Gao, Y.; Zhou, Y.; Zhou, X.; Yin, X.; Pan, C.; Yang, C.; Wang, H.; Chen, G.; Wang, L. High-Performance n-Type Thermoelectric Composites of Acridones with Tethered Tertiary Amines and Carbon Nanotubes. *J. Mater. Chem. A* **2018**, 6, 20161–

(27)   Benazzi, E.; Rettenmaier, K.; Berger, T.; Caramori, S.; Berardi, S.; Argazzi, R.; Prato, M.; Syrgiannis, Z. Photoelectrochemical Properties of SnO_2 Photoanodes Sensitized by Cationic Perylene-Di-Imide Aggregates for Aqueous HBr Splitting. *J. Phys. Chem. C* **2020**, 124, 1317–1329.

(28)   Milton, M.; Cheng, Q.; Yang, Y.; Nuckolls, C.; Hernández Sánchez, R.; Sisto, T. J. Molecular Materials for Nonaqueous Flow Batteries with a High Coulombic Efficiency and Stable Cycling. *Nano Lett.* **2017**, 17, 7859–7863.

(29)   Scaccabarozzi, A. D.; Basu, A.; Aniés, F.; Liu, J.; Zapata-Arteaga, O.; Warren, R.; Firdaus, Y.; Nugraha, M. I.; Lin, Y.; Campoy-Quiles, M.; Koch, N.; Müller, C.; Tsetseris, L.; Heeney, M.; Anthopoulos, T. D. Doping Approaches for Organic Semiconductors. *Chem. Rev.* **2021**, 122, 4420-4492.

(30)   Würthner, F.; Saha-möller, C. R.; Fimmel, B.; Ogi, S.; Leowanawat, P.; Schmidt, D. Perylene Bisimide Dye Assemblies as Archetype Functional Supramolecular Materials. *Chem. Rev.* **2016**, 116, 962–1052.

(31)   Russ, B.; Robb, M. J.; Brunetti, F. G.; Miller, P. L.; Perry, E. E.; Patel, S. N.; Ho, V.; Chang, W. B.; Urban, J. J.; Chabinyc, M. L.; Hawker, C. J.; Segalman, R. A. Power Factor Enhancement in Solution-Processed Organic n-Type Thermoelectrics through Molecular Design. *Adv. Mater.* **2014**, 26, 3473–3477.

(32)   Wang, H.; Song, J.; Qu, J.; Lian, J.; Qian, P.-C.; Wong, W.-Y. R. A Novel Perylene Diimide-Based Zwitterion as the Cathode Interlayer for High-Performance Perovskite Solar Cells. *J. Mater. Chem. A* **2020**, 8, 18117–18124.

(33)   Milton, M.; Cheng, Q.; Yang, Y.; Nuckolls, C.; Hernández Sánchez, R.; Sisto, T. J. Molecular Materials for Nonaqueous Flow Batteries with a High Coulombic Efficiency and Stable Cycling. *Nano Lett.* **2017**, 17, 7859–7863.

(34)   Bonchio, M.; Syrgiannis, Z.; Burian, M.; Marino, N.; Pizzolato, E.; Dirian, K.; Rigodanza, F.; Volpato, G. A.; la Ganga, G.; Demitri, N.; Berardi, S.; Amenitsch, H.; Guldi, D. M.; Caramori, S.; Bignozzi, C. A.; Sartorel, A.; Prato, M. Hierarchical Organization of Perylene Bisimides and Polyoxometalates for Photo-Assisted Water Oxidation. *Nat. Chem.* **2019**, 11, 146–153.

(35)   Ronconi, F.; Syrgiannis, Z.; Bonasera, A.; Prato, M.; Argazzi, R.; Caramori, S.; Cristino, V.; Bignozzi, C. A. Modification of Nanocrystalline WO3 with a Dicationic Perylene Bisimide: Applications to Molecular Level Solar Water Splitting. *J. Am. Chem. Soc.* **2015**, 137, 4630–4633.

(36)   Wu, G.; Zhang, Z.; Li, Y.; Gao, C.; Wang, X.; Chen, G. Exploring High-Performance N-Type Thermoelectric Composites Using Amino- Substituted Rylene Dimides and Carbon Nanotubes. *ACS Nano* **2017**, 11, 5746–5752.

(37)   Ogle, J.; Lahiri, N.; Jaye, C.; Tassone, C. J.; Fischer, D. A.; Louie, J.; Whittaker-Brooks, L. Semiconducting to Metallic Electronic Landscapes in Defects-Controlled 2D Π-d Conjugated Coordination Polymer Thin Films. *Adv. Funct. Mater.* **2021**, 31, 2006920.

(38)   Ogle, J.; Powell, D.; Smilgies, D.-M.; Nordlund, D.; Whittaker-Brooks, L. Promoting Bandlike Transport in Well-Defined and Highly Conducting Polymer Thin Films upon Controlling Dopant Oxidation Levels and Polaron Effects. *ACS Appl. Polym. Mater.* **2021**, 3, 2938–2949.

(39)   Oh, J. H.; Sun, Y. sen; Schmidt, R.; Toney, M. F.; Nordlund, D.; Könemann, M.; Würthner, F.; Bao, Z. Interplay between Energetic and Kinetic Factors on the Ambient Stability of N-Channel Organic Transistors Based on Perylene Diimide Derivatives. *Chem. Mater.* **2009**, 21, 5508–5518.

(40)   Taborski, J.; Väterlein, P.; Dietz, H.; Zimmermann, U.; Umbach, E. NEXAFS Investigations on Ordered Adsorbate Large Aromatic Molecules Layers of Large Aromatic Molecules. *J. Electron. Spectrosc. Relat. Phenom.* **1995**, 75, 129-147.

(41)   Fratesi, G.; Lanzilotto, V.; Stranges, S.; Alagia, M.; Brivio, G. P.; Floreano, L. High Resolution NEXAFS of Perylene and PTCDI: A Surface Science Approach to Molecular Orbital Analysis. *Phys. Chem. Chem. Phys.* **2014**, 16, 14834–14844.

(42)   Powell, D.; Campbell, E. v.; Flannery, L.; Ogle, J.; Soss, S. E.; Whittaker-Brooks, L. Steric Hindrance Dependence on the Spin and Morphology Properties of Highly Oriented Self-Doped Organic Small Molecule Thin Films. *Mater. Adv.* **2021**, 2, 356–365.

(43)   Tang, C. G.; Syafiqah, M. N.; Koh, Q. M.; Zhao, C.; Zaini, J.; Seah, Q. J.; Cass, M. J.; Humphries, M. J.; Grizzi, I.; Burroughes, J. H.; Png, R. Q.; Chua, L. L.; Ho, P. K. H. Multivalent Anions as Universal Latent Electron Donors. *Nature* **2019**, 573, 519–525.

(44)   Powell, D.; Rhodes, Z.; Zhang, X.; Miller, E. J.; Jonely, M.; Hansen, K. R.; Nwachukwu, C. I.; Roberts, A. G.; Wang, H.; Noriega, R.; Minteer, S. D.; Whittaker-Brooks, L. Photoactivation

Properties of Self-n-Doped Perylene Diimides: Concentration-Dependent Radical Anion and Dianion Formation. *ACS Mater. Au* **2022**, 2, 482-488.

(45)   Reilly, T. H.; Hains, A. W.; Chen, H. Y.; Gregg, B. A. A Self-Doping, O_2-Stable, n-Type Interfacial Layer for Organic Electronics. *Adv. Energy Mater.* **2012**, 2, 455–460.

(46)   Hestand, N. J.; Spano, F. C. Expanded Theory of H- and J - Molecular Aggregates: The Effects of Vibronic Coupling and Intermolecular Charge Transfer. *Chem. Rev.* **2018**, 118, 7069–7163.

(47)   Hestand, N. J.; Spano, F. C. Molecular Aggregate Photophysics beyond the Kasha Model: Novel Design Principles for Organic Materials. *Acc. Chem. Res.* **2017**, 50, 341–350.

(48)   Gosztola, D.; Niemczyk, M. P.; Svec, W.; Lukas, A. S.; Wasielewski, M. R. Excited Doublet States of Electrochemically Generated Aromatic Imide and Diimide Radical Anions. *J. Phys. Chem. A* **2000**, 104, 6545–6551.

(49)   Kazmaier, P. M.; Hoffmann, R. A Theoretical Study of Crystallochromy. Quantum Interference Effects in the Spectra of Perylene Pigments. *J. Am. Chem. Soc.* **1994**, 116, 9684–9691.

(50)   Braun, S.; Salaneck, W. R.; Fahlman, M. Energy-Level Alignment at Organic/Metal and Organic/Organic Interfaces. *Adv. Mater.* **2009**, 21, 1450–1472.

(51)   Jung, M. C.; Raga, S. R.; Ono, L. K.; Qi, Y. Substantial Improvement of Perovskite Solar Cells Stability by Pinhole-Free Hole Transport Layer with Doping Engineering. *Sci. Rep.* **2015**, 5, 1-5.

(52)   Bin, Z.; Dong, G.; Wei, P.; Liu, Z.; Zhang, D.; Su, R.; Qiu, Y.; Duan, L. Making Silver a Stronger N-Dopant than Cesium via in Situ Coordination Reaction for Organic Electronics. *Nat. Commun.* **2019**, 10, 1-7.

(53)   Marchini, M.; Gualandi, A.; Mengozzi, L.; Franchi, P.; Lucarini, M.; Cozzi, P. G.; Balzani, V.; Ceroni, P. Mechanistic Insights into Two-Photon-Driven Photocatalysis in Organic Synthesis. *Phys. Chem. Chem. Phys.* **2018**, 20, 8071–8076.

(54)   Matsunaga, Y.; Goto, K.; Kubono, K.; Sako, K.; Shinmyozu, T. Photoinduced Color Change and Photomechanical Effect of Naphthalene Diimides Bearing Alkylamine Moieties in the Solid State. *Chem. Eur. J.* **2014**, 20, 7309–7316.

(55)   Russ, B.; Robb, M. J.; Popere, B. C.; Perry, E. E.; Mai, C.-K.; Fronk, S. L.; Patel, S. N.; Mates, T. E.; Bazan, G. C.; Urban, J. J.; Chabinyc, M. L.; Hawker, C. J.; Segalman, R. A. Tethered Tertiary Amines as Solid-State n-Type Dopants for Solution-Processable Organic Semiconductors. Chem. Sci. **2016**, 7, 1914–1919.

(56)   Rosso, C.; Filippini, G.; Prato, M. Use of Perylene Diimides in Synthetic Photochemistry. *Eur. J. Org. Chem.* **2021**, 2021, 1193-1200.

(57)   Wang, Z.; Zheng, N.; Zhang, W.; Yan, H.; Xie, Z.; Ma, Y.; Huang, F.; Cao, Y. Self-Doped, n-Type Perylene Diimide Derivatives as Electron Transporting Layers for High-Efficiency Polymer Solar Cells. *Adv. Energy Mater.* **2017**, 7, 1–7.

(58)   Snyder, G. J.; Toberer, E. S. Complex Thermoelectric Materials. *Nat. Mater.* **2008**, 7, 105–114.

(59)   Zaumseil, J.; Sirringhaus, H. Electron and Ambipolar Transport in Organic Field-Effect Transistors. *Chem. Rev.* **2007**, 107, 1296-1323.

(60)   Facchetti, A.; Yoon, M.-H.; Marks, T. J. Gate Dielectrics for Organic Field-Effect Transistors: New Opportunities for Organic Electronics. *Adv. Mater.* **2005**, 17, 1705–1725.

(61)   Liu, C.; Xu, Y.; Noh, Y. Y. Contact Engineering in Organic Field-Effect Transistors. *Mater. Today*. 2015, 18, 79-96.

(62)   Chua, L.-L.; Zaumseil, J.; Chang, J.-F.; Ou, E. C.-W.; Ho, P. K.-H.; Sirringhaus, H.; Friend, R. H. General Observation of N-Type Field-Effect Behaviour in Organic Semiconductors. *Nature* **2005**, 434, 194–199.

(63)   Savenije, T. J.; Ferguson, A. J.; Kopidakis, N.; Rumbles, G. Revealing the Dynamics of Charge Carriers in Polymer:Fullerene Blends Using Photoinduced Time-Resolved Microwave Conductivity. *J. Phys. Chem. C* **2013**, 117, 24085–24103.

(64)   Labram, J. G.; Chabinyc, M. L. Recombination at High Carrier Density in Methylammonium Lead Iodide Studied Using Time-Resolved Microwave Conductivity. *J. Appl. Phys*. **2017**, 122, 065501.

(65)   Knupfer, M. Exciton Binding Energies in Organic Semiconductors. *Appl. Phys. A* **2003**, 77, 623–626.

(66)   Basak, D.; Pal, D. S.; Sakurai, T.; Yoneda, S.; Seki, S.; Ghosh, S. Cooperative Supramolecular Polymerization of a Perylene Diimide Derivative and Its Impact on Electron-Transporting Properties. *Phys. Chem. Chem. Phys.* **2017**, 19, 31024–31029.

(67)   Hong, M. J.; Labram, J. G. Inter-Sample and Intra-Sample Variability in Electronic Properties of Methylammonium Lead Iodide. *Adv. Funct. Mater.* **2021**, 31, 2101843.

TOC